PHYSICAL REVIEW B **99**, 184407 (2019)

Local spin moments, valency, and long-range magnetic order in monocrystalline and ultrathin films of $Y_3Fe_5O_{12}$ garnet

Y. Y. Chin,[1,2,*] H.-J. Lin,[2] Y. -F. Liao,[2] W. C. Wang,[2] P. Wang,[3] D. Wu,[3] A. Singh,[2] H.-Y. Huang,[2] Y.-Y. Chu,[2] D. J. Huang,[2] K.-D. Tsuei,[2] C. T. Chen,[2] A. Tanaka,[4] and A. Chainani[2]

[1]*Department of Physics, National Chung Cheng University, Chiayi 62102, Taiwan*
[2]*National Synchrotron Radiation Research Center, Hsinchu 30076, Taiwan*
[3]*Department of Physics, National Laboratory of Solid State Microstructures, Nanjing University, Nanjing 210093, China*
[4]*Department of Quantum Matter, ADSM, Hiroshima University, Higashi-Hiroshima 739-8530, Japan*

(Received 25 March 2019; published 9 May 2019)

We investigate and compare the electronic structure of a bulk single crystal of $Y_3Fe_5O_{12}$ garnet [YIG, a high-T_C (=560 K) ferrimagnet] with that of an epitaxial ultrathin (3.3 nm) film of YIG with a reduced ferrimagnetic temperature $T_C = 380$ K, using bulk-sensitive hard x-ray photoelectron spectroscopy (HAXPES), x-ray absorption spectroscopy (XAS), and x-ray magnetic circular dichroism (XMCD). The Fe $2p$ HAXPES spectrum of the bulk single crystal exhibits a purely trivalent Fe^{3+} state for octahedral and tetrahedral sites. The Fe $3s$ spectrum shows a clear splitting which allows us to estimate the on-site Fe $3s$-$3d$ exchange interaction energy. The valence band HAXPES spectrum shows Fe $3d$, O $2p$, and Fe $4s$ derived features and a band gap of ~2.3 eV in the occupied density of states, consistent with the known optical band gap of ~2.7 eV. Fe L-edge XAS identifies the octahedral Fe^{3+} and tetrahedral Fe^{3+} site features. XMCD spectra at the Fe $L_{2,3}$ edges show that bulk single-crystal YIG exhibits antiferromagnetic coupling between the octahedral- and tetrahedral-site spins. The calculated Fe $2p$ HAXPES, Fe L-edge XAS, and XMCD spectra using full multiplet cluster calculations match well with the experimental results and confirm the full local spin moments. In contrast, HAXPES, XAS, and XMCD of the Pt/YIG (3.3 nm) ultrathin epitaxial film grown by a pulsed laser deposition method show a finite Fe^{2+} contribution and a reduced Fe^{3+} local spin moment. The Fe^{2+} state is attributed to a combination of oxygen deficiency and charge transfer effects from the Pt capping layer to the ultrathin film. However, the conserved XMCD spectral shape for the ultrathin film indicates that the 3.3-nm epitaxial film is genuinely ferrimagnetic, in contrast to recent studies on films grown by radio-frequency magnetron sputtering which have shown a magnetic dead layer of ~6 nm. The presence of Fe^{2+} and the reduced local spin moment in the epitaxial ultrathin film lead to a reduced Curie temperature, quantitatively consistent with well-known mean-field theory. The results establish a coupling of the local Fe spin moments, valency, and long-range magnetic ordering temperature in bulk single crystal and epitaxial ultrathin-film YIG.

DOI: 10.1103/PhysRevB.99.184407

I. INTRODUCTION

Spintronics, or spin-based electronics, relies upon reproducible and robust transport of spin and charge for device operation. However, recent studies have identified pure spin currents which could efficiently transport spin angular momentum without an accompanying charge current. This would lead to the absence of an Oersted field and lower Joule heating losses [1–8] and promises new functionalities as well as energy savings. In order to generate and manipulate pure spin currents, bilayers composed of a normal metal (NM)/ferromagnetic material with a nonmagnetic layer have been extensively investigated, and fascinating phenomena such as spin pumping [3,4], the spin Seebeck effect (SSE) [5], the spin Hall effect (SHE) [6,7], and the inverse spin Hall effect [8] were recently reported. A pure spin current could be generated by a thermal gradient in the SSE, while a nonmagnetic metal with strong spin-orbit coupling, such as Pt, could convert a charge current into a spin current in the SHE. More interestingly, heterostructures with a ferro- or ferrimagnetic insulator (FMI) layer have attracted significant attention because only magnetic excitations (spin currents) are expected to propagate in the FMI layer, leading to a natural separation of spin current from charge current. The ferrimagnet $Y_3Fe_5O_{12}$ with a $T_C = 560$ K is one such insulating oxide, and consequently, the bilayer $Pt/Y_3Fe_5O_{12}$ has become a prototype for investigating spin-current phenomena. Furthermore, recent studies reported an unconventional Hall effect depending on the magnetic field, implying the importance of the interface between Pt and $Y_3Fe_5O_{12}$ [9–13].

$Y_3Fe_5O_{12}$ (YIG) is an extremely important material for ultrahigh-frequency optical modulators, femtosecond photomagnetic switching devices, and microwave applications. It also shows giant magnetoelectric and magnetocapacitance effects and exhibits Bose-Einstein condensation of magnons [14,15]. YIG crystallizes in a cubic structure ($Ia3d$) with magnetically active Fe^{3+} ions in 16a octahedral (O_h) sites and 24d tetrahedral (T_d) sites. It exhibits ferrimagnetic order below $T_C = 560$ K with antiparallel Fe spins due to

---

[*] yiyingchin@ccu.edu.tw

superexchange on the octahedral:tetrahedral sites in a 2:3 ratio with the magnetic easy axis along the 111 direction. Moreover, because it exhibits low magnetic damping and is a very good insulator (band gap of ~2.7 eV) [16], YIG is a favorite choice for generating pure spin currents via a thermal gradient. It was demonstrated that the dc magnetic moment current in YIG could reach a value of $10^{24}\mu_B/\mathrm{cm}^2$ [17].

Although bulk YIG shows only weak magnetic anisotropy, a recent study indicated the presence of perpendicular magnetic anisotropy in Pt/YIG thin films [18]. Moreover, the deviation between the bulk magnetization and the longitudinal spin Seebeck effect was attributed to the near-surface uniaxial magnetic anisotropy, which is intrinsic to YIG [18]. More significantly, the threshold current for exciting spin waves in Pt/YIG bilayer films is 2–3 orders of magnitude lower than what is expected for bulk YIG. It was theoretically shown that the strong reduction in threshold current is due to an easy-axis surface anisotropy, which also increases the power of the spin wave excitation by at least 2 orders of magnitude [19]. However, in a recent study using polarized neutron reflectometry, the authors concluded that the interface of Pt/YIG films can become nonmagnetic, and this will have important repercussions for the inverse SHE [20]. It is also known that the Curie temperature of YIG films can get reduced even for high-crystalline-quality epitaxial films [21]. Most importantly, in a recent study of epitaxial films grown by radio-frequency magnetron sputtering, the YIG films grown on $Gd_3Ga_5O_{12}$ (GGG) (111) substrates showed a magnetic dead layer of ~6 nm at the interface [22]. Thus, it is extremely important to carry out a spectroscopic characterization of the electronic structure and its relation to the magnetic properties of YIG films in bilayers. Further, it is necessary to compare it with the electronic structure of bulk single-crystal YIG using the same techniques. This would help us to identify the best conditions required for developing high-quality films for device applications.

In this work, we study single-crystal YIG(111), Pt/YIG(111), and Cu/YIG(111) epitaxial thin films using hard x-ray photoelectron spectroscopy (HAXPES) and Fe $L_{2,3}$ x-ray absorption spectroscopy (XAS) and x-ray magnetic circular dichroism (XMCD). HAXPES is ideally suited for bulk sensitive core-level and occupied valence band studies of electronic structure [23–25]. On the other hand, XAS and XMCD are well suited to studying the site- and orbital-selective unoccupied density of states and for determining element-specific orbital and spin moments [26]. Our results show the presence of Fe^{2+} and reduced Fe spin moments in the epitaxial ultrathin film compared to the pure Fe^{3+} and the full spin moment seen in the bulk single crystal. This causes a reduced Curie temperature compared to the bulk single crystal but is quantitatively consistent with well-known mean-field theory. The results indicate a direct coupling of the local Fe spin moments, valency, and long-range magnetic ordering temperature in the bulk single crystal as well as in epitaxial ultrathin-film YIG.

II. EXPERIMENTS

The YIG bulk single crystal was obtained commercially. Pt/YIG(111) and Cu/YIG(111) ultrathin films were epitaxially grown on GGG(111) substrates using pulsed laser deposition by applying a KrF excimer laser at a repetition of 4 Hz and a laser fluence of 2.7 J/cm^2. The growth temperature and oxygen pressure were 740 °C and 0.07 Torr, respectively. Clear *in situ* reflection high-energy electron diffraction (RHEED) patterns were observed during deposition, indicating the single crystallinity of the YIG films. The YIG thickness was estimated to be 3.3 nm for Pt/YIG and for Cu/YIG epitaxial films from calibrated RHEED oscillations. The film quality was further confirmed by x-ray diffraction. The YIG films were transferred into another vacuum chamber to deposit Pt/Cu films by dc magnetron sputtering. The thickness of the Pt and Cu capping layer was 3 nm. The growth rates of the YIG films and the Pt/Cu capping layers were also determined by x-ray reflectivity measurements, and the characterization procedures were reported in a recent study [27]. The Fe $L_{2,3}$ XAS and XMCD experiments were carried out at the BL11A beamline of the National Synchrotron Radiation Research Center in Taiwan. The Fe $L_{2,3}$ XAS and XMCD spectra were collected at room temperature in the total-electron yield mode with an energy resolution of better than 0.3 eV. Fe_2O_3 and NiO single crystals were measured simultaneously in a separated chamber to calibrate the photon energy with an accuracy better than 10 meV. HAXPES experiments ($h\nu = 6500$ eV) were performed at room temperature at the Taiwan beamline BL12XU of SPring-8 in Hyogo, Japan. The overall energy resolution was 0.35 eV, estimated from a fit to the Fermi edge of silver, which was also used to calibrate the binding energy.

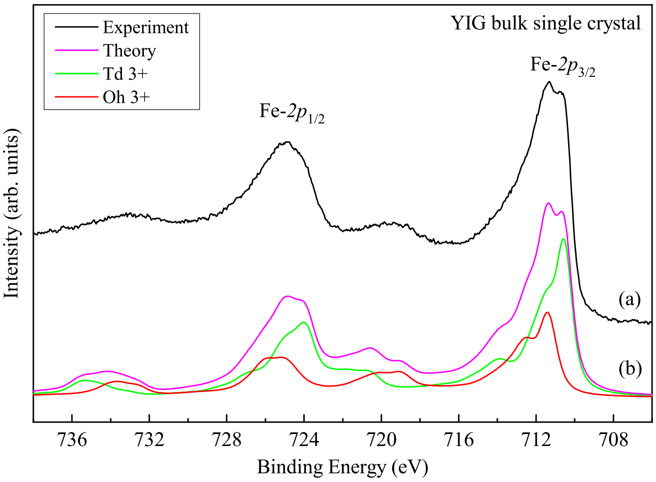

FIG. 1. (a) The Fe $2p$ HAXPES spectra of $Y_3Fe_5O_{12}$ bulk single crystal at room temperature. (b) The theoretical simulation of the HAXPES spectrum of YIG single crystal by the configuration-interaction cluster calculations.

III. RESULTS AND DISCUSSION

A. HAXPES Fe 2*p* results of bulk single crystal

The Fe $2p$ HAXPES spectrum of the YIG bulk single crystal is presented in Fig. 1(a). The spectrum consists of the $2p_{3/2}$ and $2p_{1/2}$ spectral features due to spin-orbit splitting. The $2p_{3/2}$ main peak consists of two features, positioned at binding energies (BEs) of 710.5 and 711.5 eV and a satellite

TABLE I. The parameters (in eV) for simulating the Fe $2p$ HAXPES spectrum of the YIG bulk single crystal.

	U_{dd}	U_{pd}	Δ	10 Dq	V_{eg}	V_{t2g}
T_d Fe^{3+}	6.0	7.5	2.0	−0.4	2.82	1.72
O_h Fe^{3+}	6.0	7.5	2.0	0.9	1.27	2.38

feature at about 720 eV. Similarly, the $2p_{1/2}$ main peak consists of two features, positioned at binding energies of 724.5 and 725.5 eV and a satellite feature at about 733.5 eV. In order to understand the origin of the spectral features, we carried out model configuration interaction cluster calculations [28,29] for the Fe $2p$ spectrum, including full atomic multiplets for octahedral FeO_6 and tetrahedral FeO_4 clusters. The basis states used for the calculations consist of a linear combination of the d^5, $d^6\underline{L}^1$, and $d^7\underline{L}^2$ states for Fe^{3+}. The electronic parameters for the calculations are the on-site Coulomb energy U_{dd}, the charge transfer energy Δ, the Fe $3d$-O $2p$ hybridization strength V, the crystal field splitting 10 Dq, and the Coulomb interaction in the presence of a $2p$ core hole U_{pd}. The parameters were optimized to give the best match with the experimental data, and the results are shown along with the experimental spectrum. The bulk single-crystal Fe $2p$ spectrum can be simulated nicely using a combination of O_h and T_d Fe^{3+} in a 2:3 ratio, consistent with the chemical formula. The two features of the main peak are assigned to the octahedral and tetrahedral Fe^{3+} sites, respectively. The electronic structure parameters obtained from the cluster calculations are listed in Table I. It is understood that YIG is a typical charge transfer insulator with a small charge transfer energy ($\Delta = 2$ eV), large on-site Coulomb energy ($U_{dd} = 6$ eV), and strong hybridization ($V_{eg} = 2.82$ eV and $V_{t2g} = 2.38$ eV for T_d and O_h sites, respectively) between the Fe $3d$ and O $2p$ ligand states. The charge transfer nature of YIG is consistent with the known results of other trivalent Fe^{3+} oxides, hematite (α-Fe_2O_3) [30] and maghemite (γ-Fe_2O_3) [31].

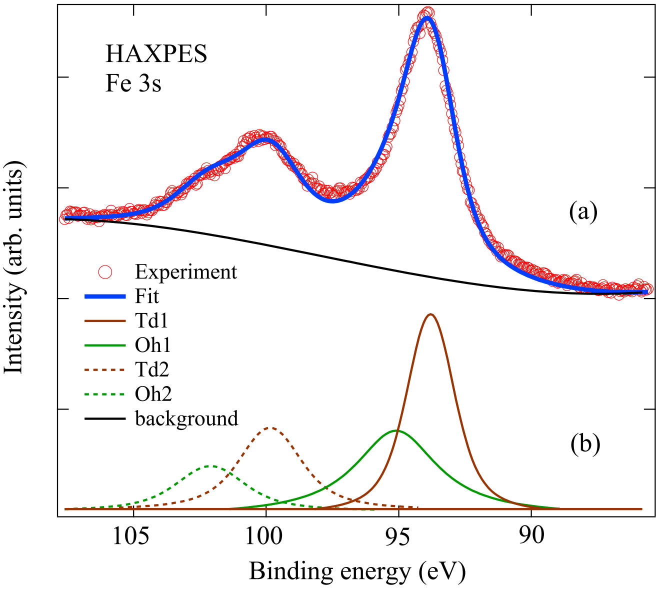

FIG. 2. (a) The Fe 3s HAXPES spectra of $Y_3Fe_5O_{12}$ bulk single crystal at room temperature. (b) The simulation consists of four peaks obtained from a fit to the HAXPES spectrum for estimating the Fe 3s multiplet splitting, as explained in the text.

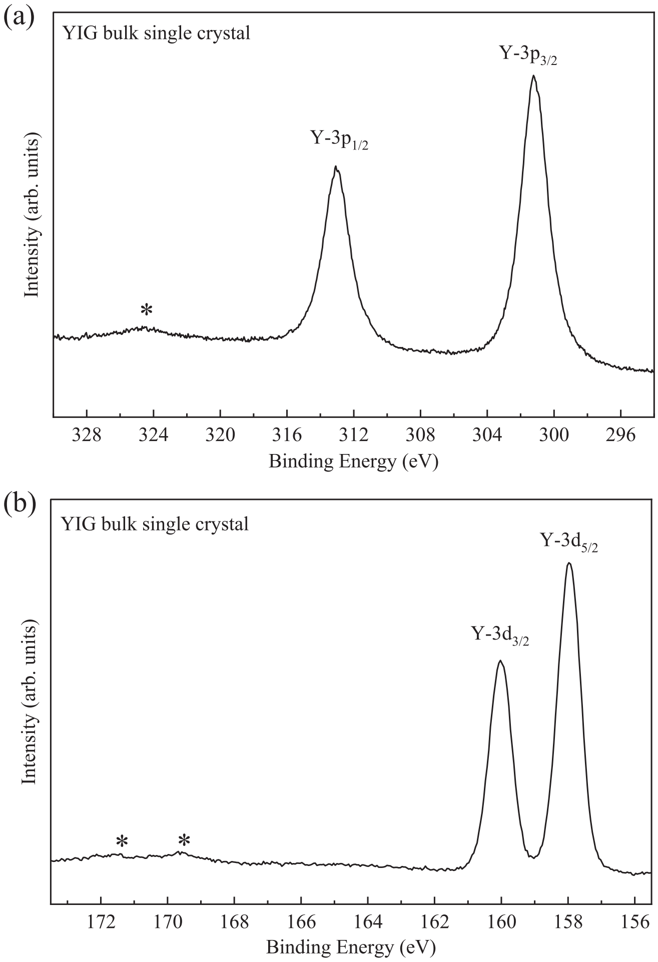

FIG. 3. (a) The Y $3p$ HAXPES spectra of $Y_3Fe_5O_{12}$ single crystal at room temperature. (b) The Y $3d$ HAXPES spectra of $Y_3Fe_5O_{12}$ bulk single crystal at room temperature. The weak plasmon features are marked by asterisks.

B. HAXPES Fe 3*s* results of bulk single crystal

In Fig. 2(a) we plot the Fe $3s$ HAXPES spectrum of bulk single-crystal YIG. The spectrum consists of two broad features, a higher-intensity feature at about 94 eV and a lower-intensity feature at 100 eV binding energy. The Fe $3s$ spectrum thus exhibits the well-known multiplet splitting due to $3s$-$3d$ exchange interaction [32]. A closer look at the higher-binding-energy feature at 100 eV shows that it consists of two peaks, which can be assigned to the tetrahedral and octahedral Fe sites. Hence, we have carried out a peak fitting to the Fe $3s$ spectrum using four peaks (Td1, Oh1, Td2, and Oh2) to accurately estimate the binding energies of the features. The fitting results are overlaid on the experimental spectrum. We obtain a splitting of ~6.0 eV for the tetrahedral Fe site and ~7.0 eV for the octahedral site. While it is known that the Fe $3s$ multiplet splitting energy $\Delta E_{3s} = (2S+1)J_{\text{eff}}$, where S is the net spin on the Fe site and J_{eff} is the effective exchange integral between the $3s$ and $3d$ states [32], the role of the intrashell correlation effects [33], final-state screening

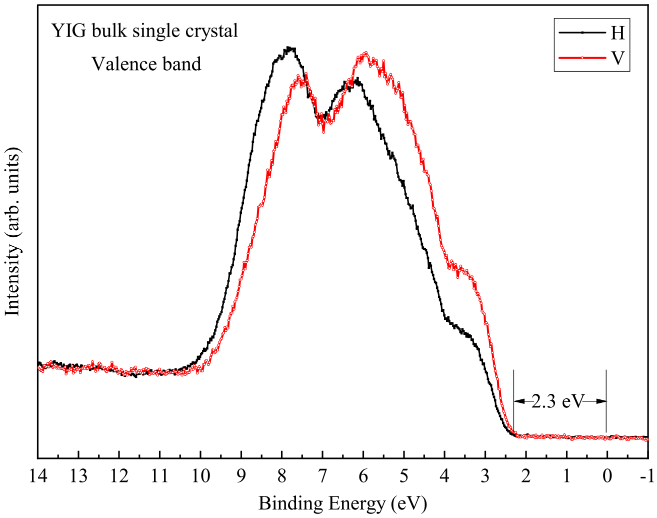

FIG. 4. The valence band HAXPES spectra of $Y_3Fe_5O_{12}$ bulk single crystal at room temperature for linear horizontal (H) and vertical (V) polarizations of the incident x rays.

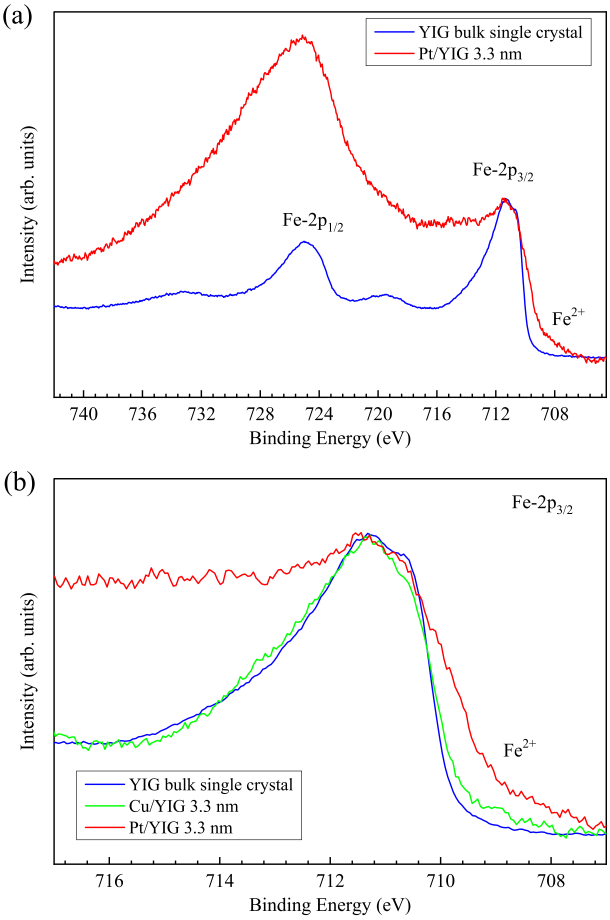

FIG. 5. (a) The wide-scan Fe $2p$ HAXPES data for bulk single-crystal YIG and Pt/YIG (3.3 nm) epitaxial film at room temperature, showing the Pt $4s$ core level overlapping the Fe $2p_{1/2}$ feature. (b) The narrow-range Fe $2p_{3/2}$ HAXPES data for YIG bulk single crystal, Cu/YIG (3.3 nm), and Pt/YIG (3.3 nm) epitaxial thin films at room temperature, showing a weak feature at low binding energy(∼708 eV) attributed to Fe^{2+} states.

[34], and charge transfer screening [35] has been recognized. More recently, a systematic study on a series of Fe compounds showed that charge transfer screening leads to a modification of ΔE_{3s} [36]. It was shown that ΔE_{3s} follows a linear relation versus $(2S+1)$ given by $\Delta E_{3s} = A + (2S+1)J_{\text{eff}}$, where A is a constant. From a fit to the experimentally observed data, it was found that $A = 0.94$ and $J_{\text{eff}} = 1.01$ eV for a series of Fe compounds. Using this relation with $A = 0.94$, as we will show later with the XMCD measurements and analysis, since $S \sim 2\mu_B$ for the tetrahedral and octahedral Fe^{3+} sites in bulk YIG, we could estimate that $J_{\text{eff}} \sim 1.0$ eV for tetrahedral Fe sites and $J_{\text{eff}} \sim 1.2$ eV for the octahedral Fe sites.

C. HAXPES Y 3*p* and 3*d* results of bulk single crystal

Figures 3(a) and 3(b) show the Y $3p$ and Y $3d$ core-level HAXPES spectra of bulk single-crystal YIG. The Y $3p$ spectrum exhibits a spin-orbit split $3p_{3/2}$ and $3p_{1/2}$ doublet at binding energies of 301 and 313 eV, respectively, while the Y $3d$ spectrum exhibits a spin-orbit split doublet at binding energies of 158 and 160 eV, respectively. The clean single peaks and the binding energies of the Y $3p$ and Y $3d$ spectra are indicative of typical Y^{3+} states. We also note that the spectra exhibit weak satellites at about 12 eV higher binding energies compared to the main peaks in both the Y $3p$ and $3d$ spectra, and these are indicative of weak plasmon features. In particular, since the splitting between the main peaks of the $3p_{3/2}$ and $3p_{1/2}$ doublet is also 12 eV, the plasmon of the main $3p_{3/2}$ feature is hidden in the main $3p_{1/2}$ feature, resulting in a small deviation of the relative spectral intensities compared to the expected ratio of 2:1 due to their degeneracies.

D. HAXPES valence band spectra of bulk single crystal

In Fig. 4, we plot the valence band HAXPES spectra obtained for horizontal and vertical linearly polarized incident x rays. The spectra show small differences for the horizontal and vertical polarization spectra. The spectra mainly consist of three broad features: the first feature is from about 2.3 to about 4 eV BE, the second is between 4.0 and 7.0 eV, and the third feature occurs between 7.0 and nearly 10.0 eV BE. The vertical polarization enhances the Fe $3d$ states, while the horizontal polarization enhances the Fe $4s$ states. In addition, based on known band structure calculations, the first feature is dominated by Fe $3d$ states, while the second feature is due to mainly O $2p$ states mixed with the Fe $3d$ states. The third feature consists of O $2p$ states mixed with Fe $4s$ states, as the Fe $4s$ states are enhanced in the horizontal incident polarization spectrum. The onset of the first feature is at 2.3 eV BE and indicates that the band gap in the occupied density of states is close to the optical band gap of YIG, which is approximately 2.7 eV [16]. This implies that the chemical potential of the bulk YIG single crystal is pinned near the bottom of its conduction band.

E. Comparative HAXPES Fe 2*p* spectra of bulk single crystal and epitaxial thin films

Next, we discuss the comparison of the HAXPES Fe $2p$ spectra of the bulk single-crystal YIG, Cu/YIG, and Pt/YIG

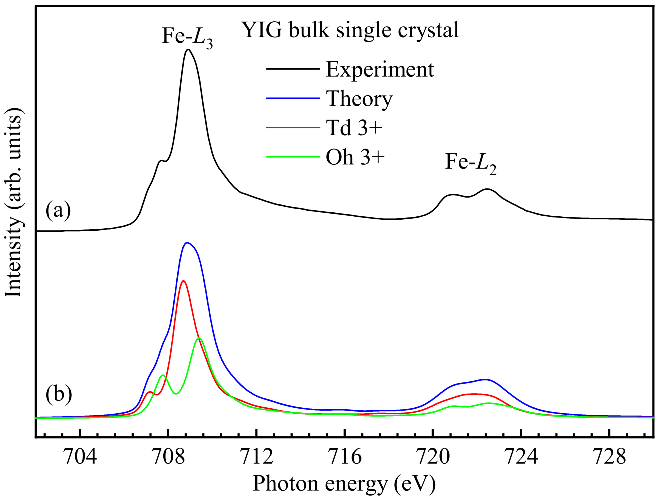

FIG. 6. (a) The Fe $L_{2,3}$ XAS data for YIG bulk single crystal at room temperature. (b) The theoretical simulation of the XAS spectrum of YIG bulk single crystal by the configuration-interaction cluster calculations.

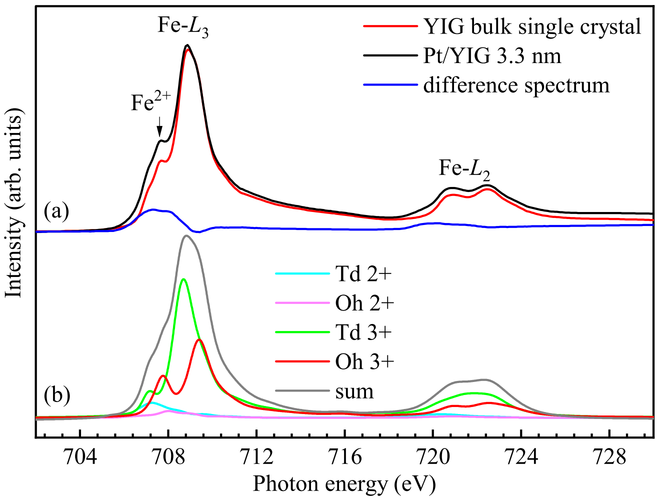

FIG. 7. (a) The Fe $L_{2,3}$ XAS spectra of $Y_3Fe_5O_{12}$ bulk single crystal and Pt/$Y_3Fe_5O_{14}$ epitaxial thin film at room temperature. (b) The simulation of the XAS spectrum of Pt/YIG epitaxial thin film by the configuration-interaction cluster calculations.

films, as shown in Fig. 5. Since the YIG films have a capping layer of 3 nm Pt/Cu metal, we could use HAXPES to measure the valency of Fe in the YIG films. However, since the Pt 4*s* core-level binding energy (∼722 eV) lies very close to the Fe $2p_{3/2}$ feature (binding energy of 710–715 eV) and it actually overlaps the Fe $2p_{1/2}$ feature [see Fig. 5(a)], we measured and compared the HAXPES of Cu/YIG and Pt/YIG films to identify the changes in the Fe $2p_{3/2}$ signal with bulk single-crystal YIG. As shown in Fig. 5(b) on an expanded scale, the presence of Fe^{2+} in Cu/YIG and Pt/YIG epitaxial thin films in the Fe $2p_{3/2}$ HAXPES spectra can be identified as a weak feature with a chemical shift to low binding energy [37]. The finite intensity observed between 708 and 710 eV indicates the existence of Fe^{2+} in the epitaxial thin films. Thus, as seen in Fig. 5(b), the Fe $2p_{3/2}$ HAXPES of the Pt/YIG 3.3-nm epitaxial film shows a higher Fe^{2+} content compared to the Cu/YIG 3.3-nm epitaxial film. This is consistent with a recent study which reported a charge transfer from the Pt capping layer compared to negligible charge transfer from a Cu capping layer in ultrathin Pt/YIG (1.6 nm) and Cu/YIG (1.6 nm) bilayers [27]. We have also confirmed there is no observable angular dependence of the spectra, indicating the absence of surface effects. This is inferred from the fact that Fe 2*p* spectra (not shown), measured with horizontal and vertical polarization at grazing incidence as well as at a 45° incidence angle, all show very similar spectral shapes. The presence of Fe^{2+} is expected to have an influence on the magnetic properties of the Pt/YIG epitaxial thin films, and to investigate this, we performed XAS and XMCD experiments on YIG bulk single crystal and Pt/YIG epitaxial thin films.

F. Comparative Fe $L_{2,3}$ XAS spectra of bulk single crystal and epitaxial thin films

The Fe $L_{2,3}$ XAS spectrum of bulk single-crystal YIG is presented in Fig. 6(a). The Fe $L_{2,3}$ XAS spectra consist of two main sets of features at ∼707–711 and ∼720–724 eV photon energies, which are the L_3 and L_2 edges derived from Fe 2*p* spin-orbit coupling. The energy positions of spectral features and their multiplet structures are characteristic of the valence state and the local symmetry of the Fe ion. We then used the same electronic parameters obtained for the Fe 2*p* photoemission spectrum to also calculate the Fe *L*-edge XAS spectrum using configuration interaction cluster calculations. We obtain a good match between the calculated and experimental spectra, as shown in Fig. 6. The main peak of the L_3 edge at 708.5 eV is dominated by tetrahedral Fe^{3+}, while the octahedral Fe^{3+} states dominate the prepeak at 707.5 eV and also contribute significantly to the main peak at the higher photon energy of 709.5 eV.

In Fig. 7(a), we plot the Fe *L*-edge XAS spectrum of the Pt/YIG epitaxial thin film compared with the YIG bulk single crystal's Fe *L*-edge XAS shown in Fig. 6. As seen in Fig. 7(a), the Pt/YIG epitaxial thin-film spectrum shows higher spectral weight at the low-energy shoulder (∼707 eV) in the Pt/YIG epitaxial thin film compared to the YIG single crystal. This implies the presence of Fe^{2+} ions in the YIG epitaxial thin film, consistent with the Fe 2*p* HAXPES spectrum shown in Fig. 5(b). In order to confirm and determine the Fe^{2+} content in the Pt/YIG epitaxial thin film, we subtracted the spectrum of the YIG bulk single crystal from that of the epitaxial thin film. The difference spectrum (blue line) is also shown in Fig. 7(a). We note that this spectral shape is different from not only the spectrum of O_h Fe^{2+} in Fe-doped MgO [38] but also that of T_d Fe^{2+} in $CaBaFe_4O_7$ [39]. However, it can be simulated by their combination and indicates the presence of both O_h Fe^{2+} and T_d Fe^{2+} in the Pt/YIG thin film. We then carried out configuration-interaction cluster calculations to simulate the Fe *L*-edge XAS spectrum. The best match to the experimental data is shown together with the experimental spectrum. The calculations indicate that the Pt/YIG 3.3-nm epitaxial film consists of ∼90% Fe^{3+} with O_h and T_d contributions in a 2:3 ratio, ∼6.9% T_d Fe^{2+} (cyan line) and ∼3.1% O_h Fe^{2+} (magenta line). The electronic structure

TABLE II. The parameters (in eV) for simulating the Fe $L_{2,3}$ XAS and XMCD data of the YIG bulk single crystal and the epitaxial thin film.

	U_{dd}	U_{pd}	Δ	10 Dq	V_{eg}	V_{t2g}	H_{ex}
				YIG bulk single crystal			
T_d Fe^{3+}	6.0	7.5	2.0	−0.4	2.82	1.72	0.04
O_h Fe^{3+}	6.0	7.5	2.0	0.9	1.27	2.38	0.04
				Pt/YIG (3.3 nm)			
T_d Fe^{3+}	6.0	7.5	2.0	−0.4	2.82	1.72	0.02
O_h Fe^{3+}	6.0	7.5	2.0	1.0	1.27	2.38	0.016
T_d Fe^{2+}	6.0	7.5	7.0	−0.4	2.82	1.72	0.007
O_h Fe^{2+}	6.0	7.5	7.0	0.6	1.27	2.38	0.007

parameters obtained from the cluster calculations are listed in Table II.

G. Comparative HAXPES O 1*s* spectra of bulk single crystal and epitaxial thin films

Having confirmed the presence of Fe^{2+} in the Pt/YIG films compared to bulk single-crystal YIG, we analyzed the O 1*s* core-level HAXPES to check the origin of Fe^{2+} in the film. As seen in Fig. 8, the O 1*s* core-level HAXPES of the bulk crystal shows a narrow single peak at about 531 eV. In contrast, the O 1*s* spectrum of the Pt/YIG film shows a broader main peak as well as a broad satellite feature extending up to a higher BE of nearly 536 eV. Since it is known that oxygen adsorption (physisorption and chemisorption) on Pt can lead to satellite features at higher BE than the main peak [40], we carried out a fitting of the spectrum to accurately identify if the satellite consists of more than one feature. The best fit is obtained by using two satellites at binding energies of 533.5 and 536.0 eV. It is known [41,42] that oxygen vacancies or defects result in a satellite typically 2 eV higher BE from the main peak. In contrast, a satellite due to oxygen physisorbed on the Pt(111) surface occurs at about 5 eV higher BE than the main peak [40]. We thus attribute the satellite at nearly 536.0 eV to physisorbed oxygen and the 533.5 eV BE satellite to oxygen vacancies in the YIG film.

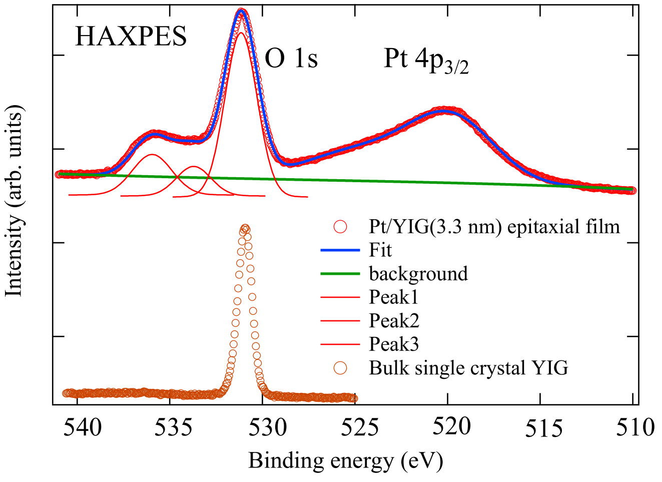

FIG. 8. The O 1*s* HAXPES spectrum of $Y_3Fe_5O_{12}$ bulk single crystal and Pt/$Y_3Fe_5O_{14}$ (3.3 nm) epitaxial thin film at room temperature. The Pt $4p_{3/2}$ feature lies close to the O 1*s* features. We have fitted the O 1*s* features of the Pt/$Y_3Fe_5O_{14}$ (3.3 nm) epitaxial thin film using Voigt functions, as shown in order to estimate the energy positions and peak widths of the features.

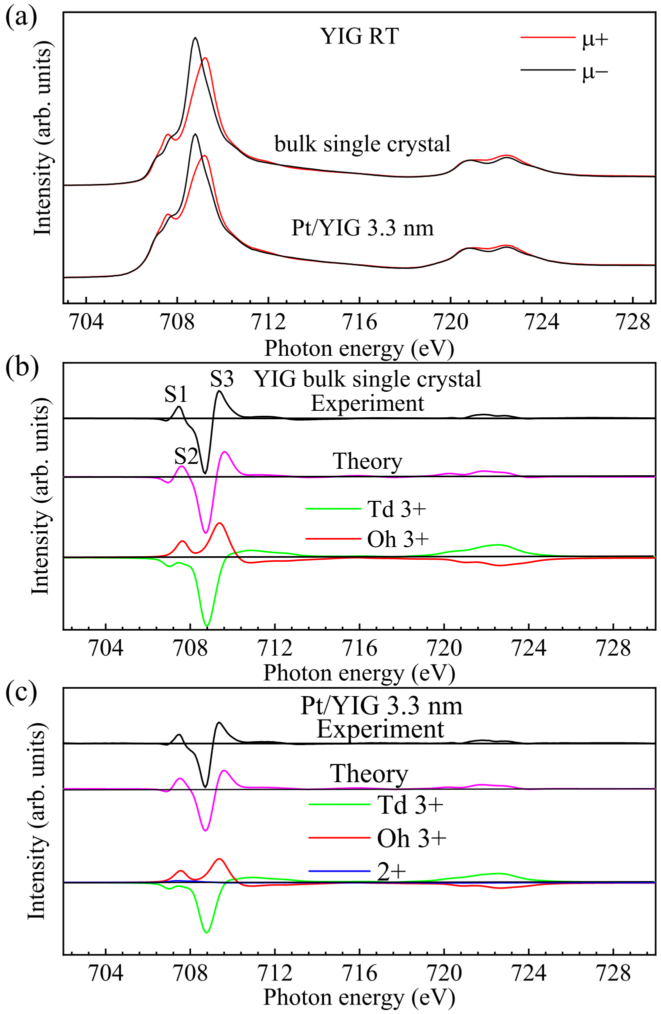

FIG. 9. (a) The Fe $L_{2,3}$ XMCD curves of $Y_3Fe_5O_{12}$ bulk single crystal and Pt/$Y_3Fe_5O_{12}$ (3.3 nm) epitaxial thin film at $T = 300$ K. The theoretical simulations for the $T = 300$ K XMCD curves of (b) the YIG single crystal and (c) Pt/YIG (3.3 nm) epitaxial thin film.

H. Comparative Fe $L_{2,3}$ XMCD results of bulk single crystal and epitaxial thin films

The $T = 300$ K Fe $L_{2,3}$ XMCD data of the YIG bulk single crystal and the Pt/YIG 3.3-nm epitaxial film are presented in Fig. 9(a). The XMCD experiments were carried out at $T = 300$ K under a 1-T magnetic field. We also tried experiments at $T = 30$ K, but the strong insulating behavior of the YIG bulk single crystal at $T = 30$ K led to spectral distortions due to charging. We first discuss the XMCD data of the bulk single-crystal YIG which show three features, S1–S3, as labeled in Fig. 9(b). By comparing our results with known XMCD curves of $GaFeO_3$ with O_h Fe^{3+} and γ-Fe_2O_3 with both T_d Fe^{3+} and O_h Fe^{3+} [43], the main Fe L_3 XMCD

TABLE III. Fe $3d$ spin moments (in units of μ_B) as determined by XMCD sum rules and XMCD simulations.

	Bulk single crystal	Pt/YIG (3.3 nm)
T$_d$ Fe^{3+}	1.97	1.46
O$_h$ Fe^{3+}	−2.03	−1.30
T$_d$ Fe^{2+}		−0.47
O$_h$ Fe^{2+}		−0.48
Per Fe	0.37	0.27
XMCD sum rules	0.35	0.27

feature in Fig. 9(b) (labeled S2) of the YIG bulk single crystal is attributed to the T$_d$ Fe^{3+}. In contrast, features S1 and S3 at lower and higher photon energies mainly come from O$_h$ Fe^{3+} and are in the direction opposite that of the T$_d$ Fe^{3+} contribution. Therefore, the XMCD signal indicates an antiparallel alignment, i.e., an antiferromagnetic coupling of the T$_d$ Fe^{3+} and O$_h$ Fe^{3+} magnetic moments, similar to what was observed in γ-Fe$_2$O$_3$ and Fe$_3$O$_4$ [43,44].

Although the orbital and spin moments could be obtained by employing the XMCD sum rules [45–47], theoretical calculations are also necessary for explaining and quantifying the observed behavior, particularly for systems with more than one valence state and/or local symmetries. For the Pt/YIG film, although it contains a finite amount of Fe^{2+} as understood from the Fe $L_{2,3}$ XAS and Fe $2p$ HAXPES spectra discussed earlier, the line shape of the XMCD signal of the epitaxial thin film is quite similar to that of the YIG bulk single crystal, implying magnetic contributions from Fe^{3+} dominate the XMCD signal. We note that in a recent study on a Pt/YIG (1.6 nm) ultrathin film [27], it was shown that the spectral shape deviates a little from that of thick YIG films (and our bulk single-crystal data). In particular, it was shown that only the T$_d$ Fe^{3+} site XMCD signal weakened, while the O$_h$ Fe^{3+} site XMCD signal did not change. This was interpreted to represent a preferential charge transfer from the Pt capping layer to the T$_d$ Fe site, resulting in T$_d$ Fe^{2+}. However, in the present case, we find that for the Pt/YIG (3.3 nm) epitaxial thin film, the spectral shape matches the bulk single-crystal XMCD signal but is uniformly weakened, and the reduction is larger than 10%, the concentration of Fe^{2+} in the film. This indicates reduced spin moments for both the T$_d$ Fe^{3+} and O$_h$ Fe^{3+} sites.

In order to quantify the magnetic dichroism of the YIG bulk single crystal as well as the Pt/YIG 3.3-nm epitaxial thin film, cluster calculations using the same parameters as those for the XAS spectra were performed, and the results are presented in Figs. 9(b) and 9(c). As shown in Fig. 9(b), there is nice agreement between the theoretical (magenta line) and experimental XMCD (black line) spectra, and thus, we can quantify the magnetic moments of Fe ions for bulk single-crystal YIG. Moreover, the site-resolved calculations shown in the bottom part of Fig. 9(b) confirm that the magnetic moments of T$_d$ Fe^{3+} and O$_h$ Fe^{3+} are indeed aligned opposite to each other. The estimated magnetic moments (listed in Table III) match very nicely with the spin moments calculated using the local spin-density approximation with on-site Coulomb energy U [48,49].

Further, as depicted in Fig. 9(c), our cluster calculations for the Pt/YIG 3.3-nm epitaxial thin film also match nicely with the experimental data. However, we needed to include the Fe^{2+} contributions to get the best match, as was discussed for the XAS data of Fig. 7. While the contribution from Fe^{2+} is quite small compared with that of Fe^{3+}, it can be expected that the Fe^{2+} ions will disturb the magnetic interactions between Fe^{3+} ions. However, more surprisingly, we find that the spin moments for the Fe^{3+} ions are also significantly reduced in the epitaxial thin film as listed in Table III. This not only explains the reduction of the XMCD signal but would also imply a reduced Curie temperature in the Pt/YIG epitaxial thin film. We measured the Curie temperature of the Pt/YIG (3.3 nm) epitaxial film, and as shown in the Supplemental Material [50], we could fit the magnetization as a function of temperature to a Bloch $T^{3/2}$ law typical of ferrimagnets. We could estimate $T_C = 380$ K for the Pt/YIG (3.3 nm) epitaxial film. Thus, the magnetization results and the XMCD spectral shape of the ultrathin film indicate that the Pt/YIG (3.3 nm) epitaxial film is genuinely ferrimagnetic. This is in contrast to recent studies on films grown by radio-frequency magnetron sputtering which have shown a magnetic dead layer of ~6 nm [22]. In fact, as discussed above, even Pt/YIG (1.6 nm) bilayer films grown by pulsed laser deposition were reported to be ferrimagnetic at room temperature [27].

Based on mean-field theory, it is known that $T_C = \mu_{\text{eff}}(C_A C_B)^{1/2}$, where μ_{eff} is the effective spin moment and C_A and C_B are Curie constants for the A and B sublattices in a ferrimagnet [51]. This equation indicates that T$_C$ is directly proportional to μ_{eff}. Indeed, the ratio of T_C for the epitaxial thin film compared to the bulk single crystal $R_{Tc} \sim 0.68$ and is close to the ratio of the effective spin moments estimated from the XMCD data: $R_{\mu 1} = 0.74 \pm 0.05$ for the T$_d$ Fe^{3+} site and $R_{\mu 2} = 0.64 \pm 0.05$ for the O$_h$ Fe^{3+} site. The small deviations for the ratio of effective moments for the T$_d$ Fe^{3+} and O$_h$ Fe^{3+} sites probably originates from the preferential charge transfer as reported for the Pt/YIG (1.6 nm) ultrathin film [27]. However, the nearly similar XMCD signal for the present case of the Pt/YIG (3.3 nm) epitaxial film suggests that the reduced spin moments on both T$_d$ Fe^{3+} and O$_h$ Fe^{3+} sites is dominated by the presence of oxygen vacancies, leading to both T$_d$ Fe^{2+} and O$_h$ Fe^{2+} sites. This can be expected to disturb and effectively weaken the exchange interaction between the T$_d$ Fe^{3+} and O$_h$ Fe^{3+} sites. Thus, the reduced T_C due to the presence of Fe^{2+} is attributed to a combination of oxygen deficiency and charge transfer effects from the Pt capping layer to the ultrathin film.

IV. CONCLUSION

In conclusion, we have carried out HAXPES, XAS, and XMCD of bulk single-crystal YIG compared to an epitaxial Pt/YIG thin-film bilayer. The Fe $2p$ HAXPES spectrum of the bulk single crystal indicates a purely trivalent Fe^{3+} state. The valence band HAXPES spectrum shows Fe $3d$, O $2p$, and Fe $4s$ derived features and a band gap of ~2.3 eV in the occupied density of states, close to the known optical band gap of 2.7 eV. Fe L-edge XAS was used to characterize the octahedral Fe^{3+} and tetrahedral Fe^{3+} site features. Fe L-edge

XMCD spectra showed that bulk single-crystal YIG exhibits antiferromagnetic coupling between the octahedral and tetrahedral sites. Moreover, the full multiplet cluster calculations of the Fe $2p$ HAXPES, Fe L-edge XAS, and XMCD spectra matched well with the experimental results and confirmed the full local spin moments. In contrast, HAXPES, XAS, and XMCD of the Pt/YIG (3.3 nm) ultrathin epitaxial film grown by a pulsed laser deposition method showed a finite Fe^{2+} contribution and a reduced Fe^{3+} local spin moment. The Fe^{2+} state is attributed to a combination of oxygen deficiency and charge transfer effects from the Pt capping layer to the ultrathin film. However, the conserved XMCD spectral shape for the ultrathin film indicates that the 3.3-nm epitaxial film is genuinely ferrimagnetic, in contrast to recent studies on films grown by radio-frequency magnetron sputtering which concluded a magnetic dead layer of $\sim$6 nm. The presence of Fe^{2+} and the reduced local spin moment in the epitaxial ultrathin film lead to a reduced Curie temperature, quantitatively consistent with known mean-field theory. The results show a coupling of the local Fe spin moments, valency, and long-range magnetic ordering temperature in bulk single-crystal and epitaxial ultrathin-film YIG.

ACKNOWLEDGMENTS

We thank Dr. Y. Tanaka for providing the single-crystal YIG and for valuable discussions. The authors would like to thank the Ministry of Science and Technology of the Republic of China, for financially supporting this research under Contracts No. MOST 106-2112-M-213-003-MY3, No. 106-2112-M-213-001-MY2, and No. 107-2112-M-194-001-MY3. The synchrotron radiation experiments were performed at the BL12XU of SPring-8 with the approval of the Japan Synchrotron Radiation Research Institute (JASRI) (Proposals No. 2016B4255 and No. 2017A4251).

[1] M. Johnson and R. H. Silsbee, Interfacial Charge-Spin Coupling: Injection and Detection of Spin Magnetization in Metals, Phys. Rev. Lett. **55**, 1790 (1985).

[2] M. Johnson, Spin Accumulation in Gold Films, Phys. Rev. Lett. **70**, 2142 (1993).

[3] R. Urban, G. Woltersdorf, and B. Heinrich, Gilbert Damping in Single and Multilayer Ultrathin Films: Role of Interfaces in Nonlocal Spin Dynamics, Phys. Rev. Lett. **87**, 217204 (2001).

[4] Y. Tserkovnyak, A. Brataas, and G. E. W. Bauer, Enhanced Gilbert Damping in Thin Ferromagnetic Films, Phys. Rev. Lett. **88**, 117601 (2002).

[5] K. Uchida, H. Adachi, T. Ota, H. Nakayama, S. Maekawa, and E. Saitoh, Observation of longitudinal spin-Seebeck effect in magnetic insulators, Appl. Phys. Lett. **97**, 172505 (2010).

[6] M. I. Dyakonov and V. I. Perel, Current-induced spin orientation of electrons in semiconductors, Phys. Lett. A **35**, 459 (1971).

[7] T. Kimura, Y. Otani, T. Sato, S. Takahashi, and S. Maekawa, Room-Temperature Reversible Spin Hall Effect, Phys. Rev. Lett. **98**, 156601 (2007).

[8] E. Saitoh, M. Ueda, H. Miyajima, and G. Tatara, Conversion of spin current into charge current at room temperature: Inverse spin-Hall effect, Appl. Phys. Lett. **88**, 182509 (2006).

[9] S. Y. Huang, X. Fan, D. Qu, Y. P. Chen, W. G. Wang, J. Wu, T. Y. Chen, J. Q. Xiao, and C. L. Chien, Transport Magnetic Proximity Effects in Platinum, Phys. Rev. Lett. **109**, 107204 (2012).

[10] S. Shimizu, K. S. Takahashi, T. Hatano, M. Kawasaki, Y. Tokura, and Y. Iwasa, Electrically Tunable Anomalous Hall Effect in Pt Thin Films, Phys. Rev. Lett. **111**, 216803 (2013).

[11] B. F. Miao, S. Y. Huang, D. Qu, and C. L. Chien, Physical Origins of the New Magnetoresistance in Pt/YIG, Phys. Rev. Lett. **112**, 236601 (2014).

[12] Y. Shiomi, T. Ohtani, S. Iguchi, T. Sasaki, Z. Qiu, H. Nakayama, K. Uchida, and E. Saitoh, Interface-dependent magnetotransport properties for thin Pt films on ferrimagnetic $\mathrm{Y_3Fe_5O_{12}}$, Appl. Phys. Lett. **104**, 242406 (2014).

[13] S. Meyer, R. Schlitz, S. Geprägs, M. Opel, H. Huebl, R. Gross, and S. T. B. Goennenwein, Anomalous Hall effect in YIG/Pt bilayers, Appl. Phys. Lett. **106**, 132402 (2015).

[14] S. O. Demokritov, V. E. Demidov, O. Dzyapko, G. A. Melkov, A. A. Serga, B. Hillebrands, and A. N. Slavin, Bose-Einstein condensation of quasi-equilibrium magnons at room temperature under pumping, Nature (London) **443**, 430 (2006).

[15] D. A. Bozhko, A. A. Serga, P. Clausen, V. I. Vasyuchka, F. Heussner, G. A. Melkov, A. Pomyalov, V. S. Lvov, and B. Hillebrands, Supercurrent in a room-temperature Bose-Einstein magnon condensate, Nat. Phys. **12**, 1057 (2016).

[16] S. Wittekoek, T. J. A. Popma, J. M. Robertson, and P. F. Bongers, Magneto-optic spectra and the dielectric tensor elements of bismuth-substituted photon energies between 2.2–5.2 eV, Phys. Rev. B **12**, 2777 (1975).

[17] B. Heinrich, C. Burrowes, E. Montoya, B. Kardasz, E. Girt, Y.-Y. Song, Y. Sun, and M. Wu, Spin Pumping at the Magnetic Insulator (YIG)/Normal Metal (Au) Interfaces, Phys. Rev. Lett. **107**, 066604 (2011).

[18] K. Uchida, J. Ohe, T. Kikkawa, S. Daimon, D. Hou, Z. Qiu, and E. Saitoh, Intrinsic surface magnetic anisotropy in $\mathrm{Y_3Fe_5O_{12}}$ as the origin of low-magnetic-field behavior of the spin Seebeck effect, Phys. Rev. B. **92**, 014415 (2015).

[19] J. Xiao and G. E. W. Bauer, Spin-Wave Excitation in Magnetic Insulators by Spin-Transfer Torque, Phys. Rev. Lett. **108**, 217204 (2012).

[20] J. F. K. Cooper, C. J. Kinane, S. Langridge, M. Ali, B. J. Hickey, T. Niizeki, K. Uchida, E. Saitoh, H. Ambaye, and A. Glavic, Unexpected structural and magnetic depth dependence of YIG thin films, Phys. Rev. B **96**, 104404 (2017).

[21] J. C. Gallagher, A. S. Yang, J. T. Brangham, B. D. Esser, S. P. White, M. R. Page, K.-Y. Meng, S. Yu, R. Adur, W. Ruane, S. R. Dunsiger, D. W. McComb, F. Yang, and P. Chris Hammel, Exceptionally high magnetization of stoichiometric $\mathrm{Y_3Fe_5O_{12}}$ epitaxial films grown on $\mathrm{Gd_3Ga_5O_{12}}$, Appl. Phys. Lett. **109**, 072401 (2016).

[22] A. Mitra, O. Cespedes, Q. Ramasse, M. Ali, S. Marmion, M. Ward, R. M. D. Brydson, C. J. Kinane, J. F. K. Cooper, S. Langridge, and B. J. Hickey, Interfacial origin of the magnetisation suppression of thin film yttrium iron garnet, Sci. Rep. **7**, 11774 (2017).

[23] K. Kobayashi, M. Yabashi, Y. Takata, T. Tokushima, S. Shin, K. Tamasaku, D. Miwa, T. Ishikawa, H. Nohira, T. Hattori, Y. Sugita, O. Nakatsuka, A. Sakai, and S. Zaima, High resolution-high energy x-ray photoelectron spectroscopy using third-generation synchrotron radiation source, and its application to Si-high k insulator systems, Appl. Phys. Lett. **83**, 1005 (2003); Y. Takata, K. Tamasaku, T. Tokushima, D. Miwa, S. Shin, and T. Ishikawa, A probe of intrinsic valence band electronic structure: Hard x-ray photoemission, *ibid.* **84**, 4310 (2004); C. Dallera, L. Duò, and L. Braicovich, Looking 100 Å deep into spatially inhomogeneous dilute systems with hard x-ray photoemission, *ibid.* **85**, 4532 (2004).

[24] C. S. Fadley, X-ray photoelectron spectroscopy: From origins to future directions, Nucl. Instrum. Methods Phys. Res., Sect. A **601**, 8 (2009); A. X. Gray, C. Papp, S. Ueda, B. Balke, Y. Yamashita, L. Plucinski, J. Minar, J. Braun, E. R. Ylvisaker, C. M. Schneider, W. Pickett, H. Ebert, K. Kobayashi, and C. S. Fadley, Probing bulk electronic structure with hard X-ray angle-resolved photoemission, Nat. Mater. **10**, 759 (2011).

[25] *Hard X-Ray Photoelectron Spectroscopy (HAXPES)*, edited by J. C. Woicik, Springer Series in Surface Sciences Vol. 59 (Springer, Cham, 2016).

[26] T. Funk, A. Deb, S. J. George, H. Wang, and S. P. Cramer, X-ray magnetic circular dichroism—A high energy probe of magnetic properties, Coord. Chem. Rev. **249**, 3 (2005).

[27] P. Wang, H. Zhao, S. Liu, Y. Y. Chin, H. J. Lin, B. M. Zhang, Z. Yuan, S. W. Jiang, H. F. Ding, J. Du, Q. Y. Xu, K. Xia, and D. Wu, Reduced interfacial magnetic moment of $Y_3Fe_5O_{12}$ by capping Pt, Appl. Phys. Lett. **113**, 182402 (2018).

[28] F. M. F. de Groot, X-ray absorption and dichroism of transition metals and their compounds, J. Electron Spectrosc. Relat. Phenom. **67**, 529 (1994).

[29] A. Tanaka and T. Jo, Resonant $3d$, $3p$ and $3s$ photoemission in transition metal oxides predicted at $2p$ threshold, J. Phys. Soc. Jpn. **63**, 2788 (1994).

[30] P. S. Miedema, F. Borgatti, F. Offi, G. Panaccione, and F. M. F. de Groot, Iron $1s$ X-ray photoemission of Fe_2O_3, J. Electron Spectrosc. Relat. Phenom. **203**, 8 (2015).

[31] J. Rubio-Zuazo, A. Chainani, M. Taguchi, D. Malterre, A. Serrano, and G. R. Castro, Electronic structure of FeO, γ-Fe_2O_3, and Fe_3O_4 epitaxial films using high-energy spectroscopies, Phys. Rev. B **97**, 235148 (2018).

[32] C. S. Fadley, D. A. Shirley, A. J. Freeman, P. S. Bagus, and J. V. Mallow, Multiplet Splitting of Core-Electron Binding Energies in Transition-Metal Ions, Phys. Rev. Lett. **23**, 1397 (1969).

[33] P. S. Bagus, A. J. Freeman, and F. Sasaki, Prediction of New Multiplet Structure in Photoemission Experiments, Phys. Rev. Lett. **30**, 850 (1973).

[34] B. W. Veal and A. P. Paulikas, X-Ray-Photoelectron Final-State Screening in Transition-Metal Compounds, Phys. Rev. Lett. **51**, 1995 (1983).

[35] G.-H. Gweon, J.-G. Park, and S.-J. Oh, Final-state screening effect in the $3s$ photoemission spectra of Mn and Fe insulating compounds, Phys. Rev. B **48**, 7825 (1993).

[36] F. Bondino, E. Magnano, M. Malvestuto, F. Parmigiani, M. A. McGuire, A. S. Sefat, B. C. Sales, R. Jin, D. Mandrus, E. W. Plummer, D. J. Singh, and N. Mannella, Evidence for Strong Itinerant Spin Fluctuations in the Normal State of $CeFeAsO_{0.89}F_{0.11}$ Iron-Oxypnictide Superconductors, Phys. Rev. Lett. **101**, 267001 (2008).

[37] T. Yamashita, and P. Hayes, Analysis of XPS spectra of Fe^{2+} and Fe^{3+} ions in oxide materials, Appl. Surf. Sci. **254**, 2441 (2008).

[38] T. Haupricht, R. Sutarto, M. W. Haverkort, H. Ott, A. Tanaka, H. H. Hsieh, H.-J. Lin, C. T. Chen, Z. Hu, and L. H. Tjeng, Local electronic structure of Fe^{2+} impurities in MgO thin films: Temperature-dependent soft x-ray absorption spectroscopy study, Phys. Rev. B **82**, 035120 (2010).

[39] N. Hollmann, M. Valldor, H. Wu, Z. Hu, N. Qureshi, T. Willers, Y.-Y. Chin, J. C. Cezar, A. Tanaka, N. B. Brookes, and L. H. Tjeng, Orbital occupation and magnetism of tetrahedrally coordinated iron in $CaBaFe_4O_7$, Phys. Rev. B **83**, 180405(R) (2011).

[40] Y. S. Kim, A. Bostwick, E. Rotenberg, P. N. Ross, S. C. Hong, and B. S. Mun, The study of oxygen molecules on Pt (111) surface with high resolution x-ray photoemission spectroscopy, J. Chem. Phys. **133**, 034501 (2010).

[41] K. Andersson, A. Nikitin, L. G. M. Pettersson, A. Nilsson, and H. Ogasawara, Water Dissociation on Ru(001): An Activated Process, Phys. Rev. Lett. **93**, 196101 (2004).

[42] F. Liu, C. Chen, H. Guo, M. Saghayezhian, G. Wang, L. Chen, W. Chen, J. Zhang, and E. W. Plummer, Unusual Fe-H bonding associated with oxygen vacancies at the (001) surface of Fe_3O_4, Surf. Sci. **655**, 25 (2017).

[43] J.-Y. Kim, T. Y. Koo, and J.-H. Park, Orbital and Bonding Anisotropy in a Half-Filled $GaFeO_3$ Magnetoelectric Ferrimagnet, Phys. Rev. Lett. **96**, 047205 (2006).

[44] J. A. Moyer, C. A. F. Vaz, D. A. Arena, D. Kumah, E. Negusse, and V. E. Henrich, Magnetic structure of Fe-doped $CoFe_2O_4$ probed by x-ray magnetic spectroscopies, Phys. Rev. B **84**, 054447 (2011).

[45] B. T. Thole, P. Carra, F. Sette, and G. van der Laan, X-Ray Circular Dichroism as a Probe of Orbital Magnetization, Phys. Rev. Lett. **68**, 1943 (1992).

[46] P. Carra, B. T. Thole, M. Altarelli, and X. Wang, X-Ray Circular Dichroism and Local Magnetic Fields, Phys. Rev. Lett. **70**, 694 (1993).

[47] C. T. Chen, Y. U. Idzerda, H.-J. Lin, N. V. Smith, G. Meigs, E. Chaban, G. H. Ho, E. Pellegrin, and F. Sette, Experimental Confirmation of the X-Ray Magnetic Circular Dichroism Sum Rules for Iron and Cobalt, Phys. Rev. Lett. **75**, 152 (1995).

[48] A. Rogalev, J. Goulon, F. Wilhelm, Ch. Brouder, A. Yaresko, J. Ben Youssef, and M. V. Indenbom, Element selective X-ray magnetic circular and linear dichroisms in ferrimagnetic yttrium iron garnet films, J. Magn. Magn. Mater. **321**, 3945 (2009).

[49] W. Y. Ching, Z. Gu, and Y.-N. Xu, Theoretical calculation of the optical properties of $Y_3Fe_5O_{12}$, J. Appl. Phys. **89**, 6883 (2001).

[50] See Supplemental Material at http://link.aps.org/supplemental/10.1103/PhysRevB.99.184407 for the magnetic characterization of the Pt/YIG (3.3 nm) epitaxial thin film.

[51] C. Kittel, *Introduction to Solid State Physics* (Wiley, Hoboken, NJ, 2005).